Progress In Electromagnetics Research B, Vol. 92, 109–126, 2021

Optimization Design and Modeling of a Built-in Hybrid Magnetic Bearing with a Permanent Magnet Motor

Yanjun Yu*, Qianwen Xiang, and Weiyu Zhang

Abstract—In this paper, a built-in hybrid magnetic bearing (BHMB) with a permanent magnet (PM) motor is proposed to reduce the axial length of the system. The BHMB shares the same distributed hollow rotor with an external PM motor. The structure and principle of BHMB are illustrated. The mathematic model of BHMB is deduced to design parameters, and the influences of parameters are analyzed. To improve the performance indexes of BHMB, a multi-objective optimization method based on Taguchi method is proposed. The values of parameters of BHMB can be chosen according to the proportion of each parameter. Finally, the finite element analysis (FEA) and experiment are used to verify the correctness of BHMB.

1. INTRODUCTION

Magnet bearing is a kind of high performance noncontact bearing which uses electromagnetic force to suspend the rotor in a balance position [1–3]. Because of its advantages of no friction, no wear, high precision, long life, etc., magnetic bearing is widely used in the supporting subsystems of high-speed rotating systems. Meanwhile, magnetic bearing is of great significance for special working occasions such as vacuum, cleaning, and hard-to maintain [4–8].

At present, there are three major types of magnetic bearings: active magnetic bearings (AMBs), passive magnetic bearings (PMBs), and hybrid magnetic bearings (HMBs) [9, 10]. In terms of above mentioned three magnetic bearings, HMBs have the advantages of AMBs and PMBs, in which the bias fluxes are provided by permanent magnets (PMs), thereby reducing the power loss effectively and numbers of turns of coils [11–13].

Meanwhile, the magnetic bearing is usually built into the motor to reduce the axial length of the rotor system. The radial and axial magnetic bearings were built in the 5MW PM wind turbine in [14]. An active magnetic bearing with four poles is built in the switched reluctance motor to suspend rotor in [15, 16]. Both the bias flux and control flux are provided by the suspension control windings in the active magnetic bearing, then the system power loss will be increased. In order to integrate the motor system, the double stator bearingless switched reluctance motor is constructed by combining the magnetic bearing and switched reluctance motor in [17–19]. In [20] and [21], the suspension device is also built in motor to realize levitation and rotation.

In order to shorten the rotor length, reduce the rotor vibration and system power loss, a built-in hybrid magnetic bearing (BHMB) is used to substitute the mechanical bearing in this paper. The BHMB not only has the levitation characteristics as the conventional HMB, but also has the advantages of compact structure and high integration. It shares the same rotor with the external permanent motor, and the BHMB with the external permanent motor can be regarded as an integrated structure.

The remainder of this paper is organized as follows. The structure and operational principle of the BHMB are proposed in Section 2. In Section 3, the model of suspension force about BHMB is deduced.

Received 27 November 2020, Accepted 31 March 2021, Scheduled 8 May 2021
* Corresponding author: Yanjun Yu (yuyanjun@ujs.edu.cn).
The authors are with the School of Electrical and Information Engineering, Jiangsu University, Zhenjiang 212013, China.

Then the influence of the main parameters is discussed, and the Taguchi method is used to optimize the parameters of BHMB in Section 4. In Section 5, simulations and experiments are carried out to verify the feasibility of BHMB. Finally, the conclusion is given in Section 6.

2. BASIC STRUCTURE AND PRINCIPLE OF BHMB

2.1. Structure of the BHMB

The structure of the BHMB is shown in Fig. 1, which mainly consists of a distributed hollow rotor, a stator, suspension control windings in x, y directions, and radially magnetized PMs. According to [22] and [23], the maximum deflection will most likely to occur in the middle of rotor. Further, to reduce the weight of rotor in wind turbine, eliminate the mutual influence between the internal and external magnetic fields of rotor, and improve the stiffness of rotor, a distributed hollow structure is used in the rotor. The three-dimensional graph of the distributed hollow rotor is shown in the Fig. 2.

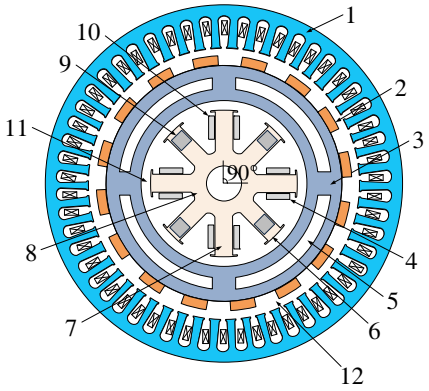

1. Stator of motor, 2. PM mounted on the rotor, 3. Rotor, 4. Suspension control windings in x direction, 5. Hollow part of rotor, 6. Bias flux pole, 7. Suspension control pole, 8. Stator of BHMB, 9. PM of BHMB, 10. Suspension control windings in y direction, 11. Air gap of BHMB, 12, Air gap of motor.

Figure 1. Structure of BHMB.

Figure 2. Three-dimensional graph of distributed hollow rotor.

As can be seen from Fig. 1, the BHMB, which contains four bias flux poles and four suspension control poles, is built in the motor and shares the distributed hollow rotor with motor. The suspension control pole and bias flux pole are arranged alternately along the circumference. The mechanical angle between the two adjacent suspension control poles is 90 degrees in space. The suspension of rotor in x and y directions is controlled by the suspension windings wound around the suspension control poles.

And the mechanical angle between the two adjacent bias poles is also 90 degrees in space. The four radial magnetized PMs are embedded in four bias flux poles, respectively.

A local flux distribution diagram of the distributed hollow rotor is shown in Fig. 3. As can be seen from Fig. 3, there are two main magnetic circuits in the system. One is the magnetic circuit of motor system provided by the PMs placed on the outer surface of rotor, and the other is the magnetic circuit created by the suspension system. The two magnetic circuits are separated by an air gap, then the interrelationships between the suspension system and motor system can be greatly reduced.

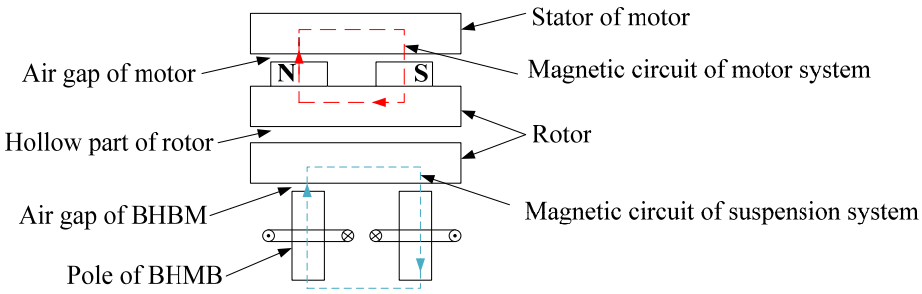

Figure 3. Local flux distribution of hollow rotor.

As shown in Fig. 1, in order to install the PM into the bias flux pole easily, the holes can be opened in the bias flux poles firstly. Then, the PMs are embedded in the holes after the rotor is installed, which can eliminate the influences between the PMs and the rotor. However, there will be leakage fluxes flowing through the two thin side walls of PM produced by the opening hole, as shown in Fig. 4(a). In order to reduce the leakage fluxes flowing through the side walls, the thickness of side wall should be minimized, and the magnetoresistance at the side walls should be increased, then the side walls are in the state of magnetic saturation, as shown in Fig. 4(b).

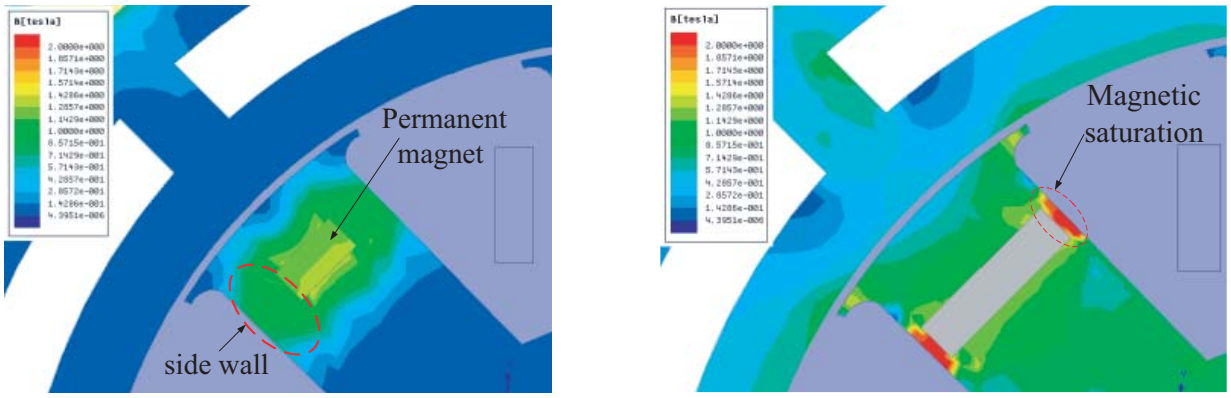

Figure 4. Magnetic field distribution of a PM in BHMB.

However, the mechanical strength and working life of the punching piece will be reduced because the side wall is too thin. Thereby the width of side wall is set to 2.5 mm according to the processing technology and the magnetic saturation of side wall.

2.2. Principle of the BHMB

As shown from Fig. 5, the bias fluxes generated by the radial magnetized PMs shown as the solid lines pass through the air gap, rotor core, suspension control pole, stator yoke, and return back to the PMs

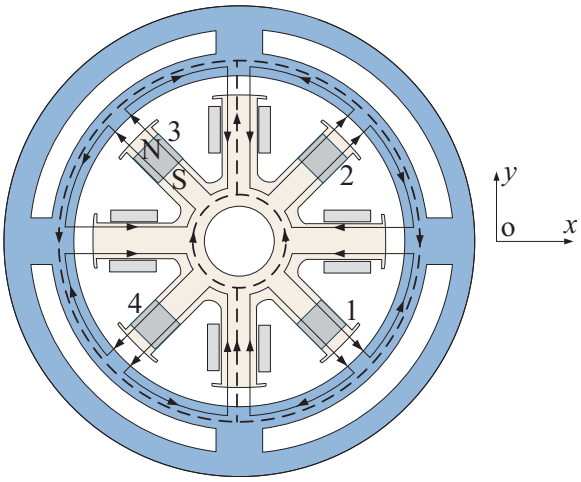

Figure 5. Schematic diagram of suspension force generation.

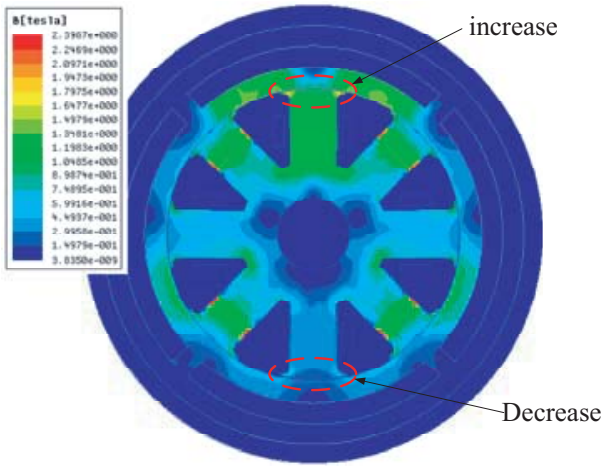

Figure 6. Magnetic field distribution with the eccentric rotor.

finally. The suspension control fluxes generated by suspension control windings shown as the dotted lines pass through the air gap, rotor core, suspension control pole, then return back. The suspension control fluxes do not pass through the bias poles because the reluctance of the PMs is very large. Therefore, the demagnetizations of the PMs influenced by the suspension control fluxes are avoided.

Take the y direction as an example to illustrate the suspension principle of BHMB. In the common state, the rotor can suspend in the equilibrium position, and the magnetic field inside the rotor is symmetrical and evenly distributed. While the rotor is shifted to $-y$ direction by disturbance, the length of air gap in $+y$ direction will be smaller than the length of air gap in $-y$ direction. Hence, the flux of air gap in $+y$ direction is larger than the flux in $-y$ direction, as shown in Fig. 6.

To make the rotor return to the equilibrium position, the suspension control currents with the same amplitude and the opposite direction are added to the corresponding control windings in $+y$ and $-y$ directions, respectively. Then, the control fluxes will subtract the bias flux in $+y$ direction and add the bias flux in $-y$ direction. The flux of air gap in $+y$ direction will be decreased, and the flux of air gap in $-y$ direction will be increased. According to the Maxwell theory [24], Maxwell force F along the $+y$ direction will be generated on the rotor. Then, the rotor will be pulled back to the equilibrium position. The principle of the suspension control in radial x direction is the same as above. Therefore, the rotor can be stably suspended in the radial 2 degrees of freedom (DOF) directions by controlling the suspension control currents.

3. ANALYSIS OF BHMB

Firstly, the models of fluxes in air gap will be deduced according to the equivalent magnetic circuit method. Moreover, several assumptions for simplicity are made as follows: 1) the permeabilities of iron are infinite; 2) the end effects and slotting are ignored; 3) the demagnetization curve of the PM is linear.

3.1. Equivalent Magnetic Circuit Model of PMs

The equivalent magnetic circuit of the bias flux of the BHMB is shown in Fig. 7. Φ_{mb1}, Φ_{mb2}, Φ_{mb3}, and Φ_{mb4} are the total fluxes provided by the four PMs to outside, respectively. $R_{mb1} \sim R_{mb4}$, $R_{m\sigma 1} \sim R_{m\sigma 4}$, and $F_{cb1} \sim F_{cb4}$ are the internal reluctances, leakage reluctances, and the MMFs of the four PMs, respectively. R_{m1}, R_{m2}, R_{m3}, and R_{mb4} are the reluctances of air gap corresponding to the four bias poles. Φ_{x1}, Φ_{x2}, Φ_{y1}, and Φ_{y2} are the fluxes flowing through the suspension control poles. R_{x1}, R_{x2}, R_{y1}, and R_{y2} are the reluctances of air gap in $+x$, $-x$, $+y$, and $-y$ directions.

According to the formula of reluctance of air gap from [25], the reluctances of air gap can be

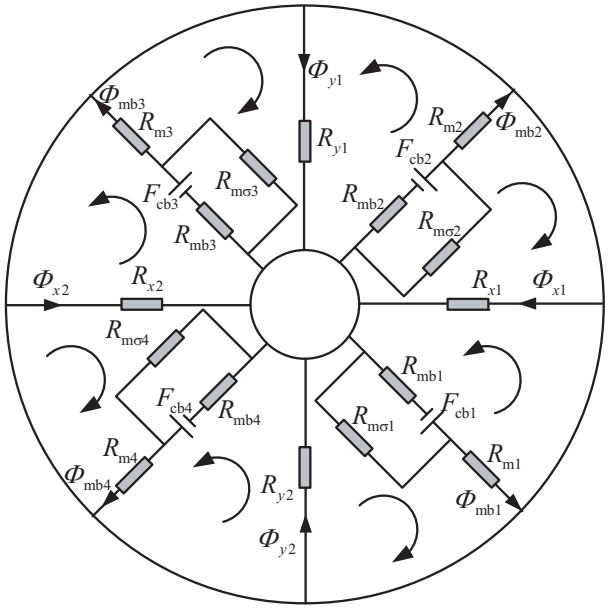

Figure 7. Equivalent magnetic circuit of the bias flux.

obtained as follows:

$$R_{x1} = \frac{x_b}{\mu_0 S_{x1}} \tag{1}$$

$$R_{x2} = \frac{2g_0 - x_b}{\mu_0 S_{x2}} \tag{2}$$

$$R_{y1} = \frac{y_b}{\mu_0 S_{y1}} \tag{3}$$

$$R_{y2} = \frac{2g_0 - y_b}{\mu_0 S_{y2}} \tag{4}$$

$$R_{m1} = \frac{d_{mb1}}{\mu_0 S_{m1}} \tag{5}$$

$$R_{m2} = \frac{d_{mb2}}{\mu_0 S_{m2}} \tag{6}$$

$$R_{m3} = \frac{2g_0 - d_{mb1}}{\mu_0 S_{m3}} \tag{7}$$

$$R_{m4} = \frac{2g_0 - d_{mb2}}{\mu_0 S_{m4}} \tag{8}$$

where μ_0 is the air permeability; x_b and y_b are the lengths of air gap in $+x$ and $+y$ directions; S_{x1}, S_{x2}, S_{y1}, and S_{y2} are the effective areas of poles in $+x$, $-x$, $+y$, and $-y$ directions; d_{mb1} and d_{mb2} are the lengths of air gaps corresponding to the bias poles 1 and 2; S_{m1}, S_{m2}, S_{m3}, and S_{m4} are the effective areas of the four bias poles, and the areas of eight poles in this paper are set:

$$S_{x1} = S_{x2} = S_{y1} = S_{y2} = S_{m1} = S_{m2} = S_{m3} = S_{m4} = S_b \tag{9}$$

Hence, the internal reluctances of PMs are:

$$R_{mb1}{=}R_{mb2} = R_{mb3} = R_{mb4} = R_{mb}{=}\frac{h_{mb}}{\mu_0 \mu_r S_b} \tag{10}$$

where μ_r is the relative permeability of PM, and h_{mb} is the length of magnetized direction of PM.

And the length of air gap corresponding to the bias pole can be approximately as follows:

$$d_{mb1} = d_{mb2}{=}g_0 + \sqrt{(x-g_0)^2 + (y-g_0)^2}\cos\beta \tag{11}$$

where β is the mechanical angle between two adjacent poles, and $\beta = 45^\circ$ in this paper.

Because the material, height and width of the two PMs placed on the flux poles are the same in this paper, the MMF of PMs can be obtained:

$$F_{cb1}{=}F_{cb2}{=}F_{cb3}{=}F_{cb4}{=}F_{cb} \tag{12}$$

where $F_{cb} = H_c h_{mb}$, H_{cb} is the coercive force of PM.

To simplify the calculation, the leakage coefficient of bias flux σ_b and total reluctances of bias poles $R_{mz1} \sim R_{mz4}$ are introduced in this paper, then the following equations can be obtained:

$$R_{mz1} = R_{mb}{+}R_{m1} \tag{13}$$

$$R_{mz2} = R_{mb}{+}R_{m2} \tag{14}$$

$$R_{mz3} = R_{mb}{+}R_{m3} \tag{15}$$

$$R_{mz4} = R_{mb}{+}R_{m4} \tag{16}$$

According to the Kirchhoff's law of magnetic circuit, the bias fluxes generated by PMs are:

$$\Phi_{x1} = \frac{F_{cb}(1/R_{mz1} + 1/R_{mz2} + 1/R_{mz3} + 1/R_{mz4})}{\sigma_b R_{x1} R_{mm}} \tag{17}$$

$$\Phi_{x2} = \frac{F_{cb}(1/R_{mz1} + 1/R_{mz2} + 1/R_{mz3} + 1/R_{mz4})}{R_{mm}\sigma_b R_{x2}} \tag{18}$$

$$\Phi_{y1} = \frac{F_{cb}(1/R_{mz1} + 1/R_{mz2} + 1/1R_{mz3} + 1/R_{mz4})}{R_{mm}\sigma_b R_{y1}} \tag{19}$$

$$\Phi_{y2} = \frac{F_{cb}(1/R_{mz1} + 1/R_{mz2} + 1/R_{mz3} + 1/R_{mz4})}{R_{mm}\sigma_b R_{y2}} \tag{20}$$

$$\Phi_{mb1} = \frac{F_{cb}(1/R_{x1} + 1/R_{x2} + 1/R_{y1} + 1/1R_{y2})}{R_{mm}\sigma_b R_{mz1}} \tag{21}$$

$$\Phi_{mb2} = \frac{F_{cb}(1/R_{x1} + 1/R_{x2} + 1/R_{y1} + 1/R_{y2})}{R_{mm}\sigma_b R_{mz2}} \tag{22}$$

$$\Phi_{mb3} = \frac{F_{cb}(1/R_{x1} + 1/R_{x2} + 1/R_{y1} + 1/R_{y2})}{R_{mm}\sigma_b R_{mz3}} \tag{23}$$

$$\Phi_{mb4} = \frac{F_{cb}(1/R_{x1} + 1/R_{x2} + 1/R_{y1} + 1/R_{y2})}{R_{mm}\sigma_b R_{mz4}} \tag{24}$$

where, $R_{mm} = \frac{1}{R_{mz1}} + \frac{1}{R_{mz2}} + \frac{1}{R_{mz3}} + \frac{1}{R_{mz4}} + \frac{1}{R_{x1}} + \frac{1}{R_{x2}} + \frac{1}{R_{y1}} + \frac{1}{R_{y2}}$.

3.2. Equivalent Magnetic Circuit Model of Control Windings

The equivalent magnetic circuit of control flux is shown in Fig. 8. $n_{xb}i_{xb}$ and $n_{yb}i_{yb}$ are the MMFs generated by suspension control windings in x and y directions, respectively; Φ_{cx1}, Φ_{cx2}, Φ_{cy1}, and Φ_{cy2} are the control fluxes in $+x$, $-x$, $+y$, and $-y$ directions, respectively.

As the equal suspension control currents with opposite direction are loaded to the corresponding control windings in $+x$ and $-x$ directions, the magnetic field distribution of BHMB is shown in Fig. 9. As can be seen from Fig. 9, the flux generated by suspension control windings in x direction does not flow through the suspension control poles in y direction. Hence, the coupling between the magnetic fields of suspension control windings in x and y directions can be ignored. Then according to the Kirchhoff's law of magnetic circuit, the control fluxes generated by suspension control windings in x and y directions are:

$$\Phi_{cx1} = \Phi_{cx2} = \frac{1}{\sigma_{cb}} \cdot \frac{n_{xb} i_{xb} \mu_0 S_b}{g_0} \tag{25}$$

$$\Phi_{cy1} = \Phi_{cy2} = \frac{1}{\sigma_{cb}} \cdot \frac{n_{yb} i_{yb} \mu_0 S_b}{g_0} \tag{26}$$

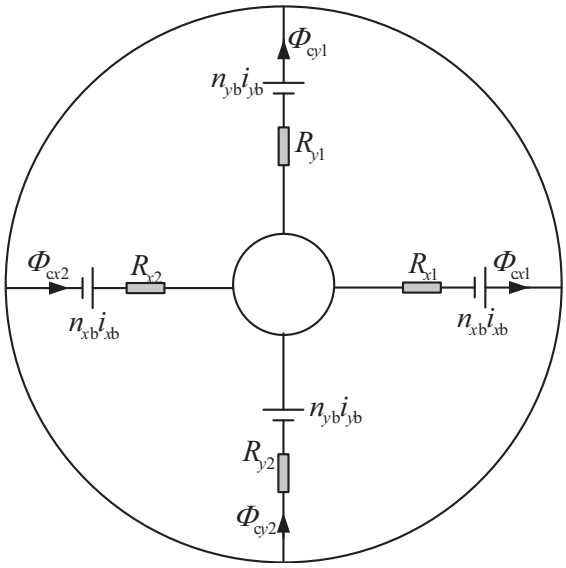

Figure 8. Equivalent magnetic circuit of the control flux.

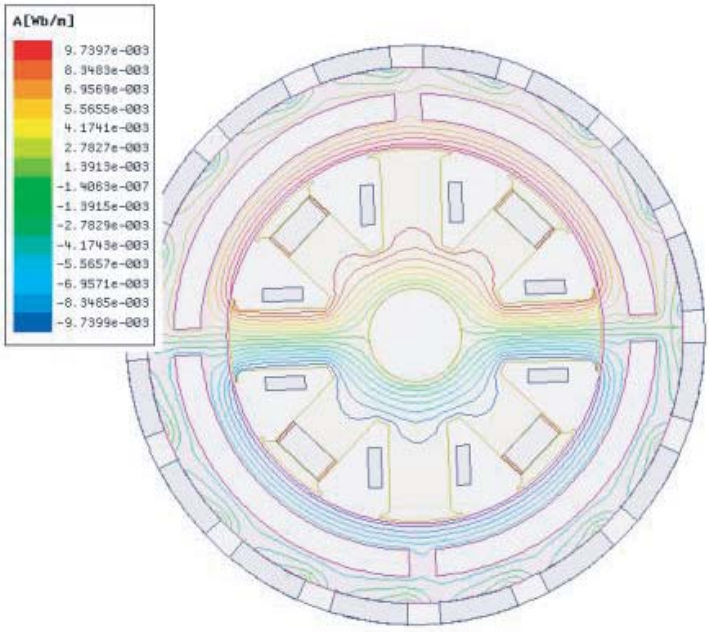

Figure 9. Magnetic field distribution of BHMB.

where σ_{cb} is the leakage coefficient of control flux, and σ_{cb} is set equal to σ_b in this paper.

3.3. Modeling of Suspension Forces in BHMB

According to the formula of flux density of air gap from [25], the flux densities of air gap corresponding to the suspension control poles and bias poles are:

$$B_{xb1} = \left\{ \frac{4F_{cb}\mu_r D_2}{\left[D_1^2 g_0 \mu_r^2 - 2D_1 D_3 g_0 h_{mb} + 4\mu_r D_2\right] x_b} + \frac{n_{xb} i_{xb}}{g_0} \right\} \times \frac{\mu_0}{\sigma_b} \tag{27}$$

$$B_{xb2} = \left\{ \frac{4F_{cb}\mu_r D_2}{\left[D_1^2 g_0 \mu_r^2 - 2D_1 D_3 g_0 h_{mb} + 4\mu_r D_2\right](2g_0 - x_b)} - \frac{n_{xb} i_{xb}}{g_0} \right\} \times \frac{\mu_0}{\sigma_b} \tag{28}$$

$$B_{yb1} = \left\{ \frac{4F_{cb}\mu_r D_2}{\left[D_1^2 g_0 \mu_r^2 - 2D_1 D_3 g_0 h_{mb} + 4\mu_r D_2\right] y_b} + \frac{n_{yb} i_{yb}}{g_0} \right\} \times \frac{\mu_0}{\sigma_b} \tag{29}$$

$$B_{yb2} = \left\{ \frac{4F_{cb}\mu_r D_2}{\left[D_1^2 g_0 \mu_r^2 - 2D_1 D_3 g_0 h_{mb} + 4\mu_r D_2\right](2g_0 - y_b)} - \frac{n_{yb} i_{yb}}{g_0} \right\} \times \frac{\mu_0}{\sigma_b} \tag{30}$$

$$B_{mb1} = B_{mb2} = \frac{-2D_1 g_0 \mu_r}{\left[D_1^2 g_0 \mu_r^2 - 2D_1 D_3 g_0 h_{mb} + 4\mu_r D_2\right]} \times \frac{\left(2h_{mb}^2 + 4g_0 h_{mb}\mu_r - D_1\mu_r^2\right) F_{cb}}{(2h_{mb} + 2g_0\mu_r + D_4)\sigma_b} \tag{31}$$

$$B_{mb3} = B_{mb4} \frac{2D_1 g_0 \mu_r}{\left[D_1^2 g_0 \mu_r^2 - 2D_1 D_3 g_0 h_{mb} + 4\mu_r D_2\right]} \times \frac{\left(2h_{mb}^2 + 4g_0 h_{mb}\mu_r - D_1\mu_r^2\right) F_{cb}}{(D_4 - 2h_{mb} - 2g_0\mu_r)\sigma_b} \tag{32}$$

$$D_1 = x_b^2 + y_b^2 - 2g_0(x_b + y_b) \tag{33}$$

$$D_2 = (h_{mb} + g_0\mu_r)(2g_0 - x_b)(2g_0 - y_b)x_b y_b \tag{34}$$

$$D_3 = h_{mb} + 2g_0\mu_r \tag{35}$$

$$D_4 = \sqrt{2}\mu_r \sqrt{2g_0^2 + x_b^2 + y_b^2 - 2g_0(x_b + y_b)} \tag{36}$$

where B_{xb1}, B_{xb2}, B_{yb1}, and B_{yb2} are the flux densities of air gap corresponding to the control poles in $+x$, $-x$, $+y$, and $-y$ directions. B_{mb1}, B_{mb2}, B_{mb3}, and B_{mb4} are the flux densities of air gap corresponding to the bias poles.

Therefore, the models of radial suspension forces in x and y directions can be obtained as follows:

$$F_{xb} = \frac{B_{xb1}^2 S_{bxy}}{2\mu_0} - \frac{B_{xb2}^2 S_{bxy}}{2\mu_0} \tag{37}$$

$$F_{yb} = \frac{B_{yb1}^2 S_{bxy}}{2\mu_0} - \frac{B_{yb2}^2 S_{bxy}}{2\mu_0} \tag{38}$$

where S_{bxy} is the projected area of the stator pole in radial direction.

$$S_{bxy} = \frac{2\sin\left(\frac{\alpha}{2}\right)}{\alpha} S_b \tag{39}$$

where α is the polar arc of the stator poles.

4. DESIGN AND OPTIMIZATION OF BHMB

4.1. Influences of Parameters on Suspension Force

The required maximum suspension force is set to 600 N in this paper. Based on the model of suspension force deduced above, the related main parameters are designed preliminarily and shown in Fig. 10 and Table 1.

As can be seen from Fig. 10, the parameters design, such as the arc length of pole shoes, the width and thickness of stator yoke, can be converted to the design of coil cavity, as shown in Fig. 11. B_{s0} is the slot width of rabbet, B_{s1} the widest length of a coil cavity, c_m the height of shoulder of a pole shoe, d_m the height of a pole shoe, and h_b the height of coil cavity. The relation between the arc length of pole shoe and slot width of rabbet is:

$$l_0 = \frac{\pi D_{s1}}{8} - B_{s0} \tag{40}$$

When the suspension control currents with the same amplitude 2.8 A and the opposite directions are loaded to the corresponding control windings in $+x$ and $-x$ directions, the relationships between the parameters of the coil cavity and the radial suspension force in x direction are shown in Fig. 12.

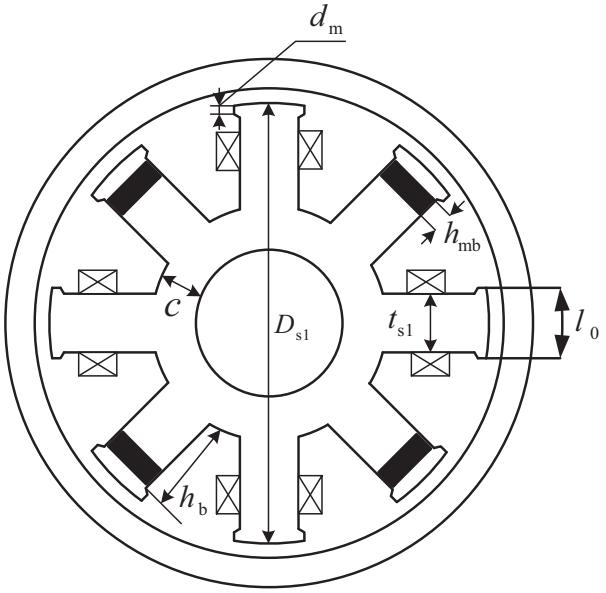

Figure 10. Parameters of BHMB.

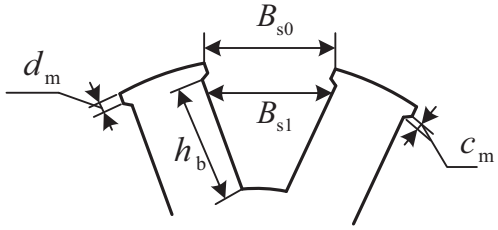

Figure 11. Dimension of coil cavity in BHMB.

Table 1. Main parameters of the BHMB.

Parameters	value	Parameters	value
Numbers of stator poles	8	Axial length of stator l_1 (mm)	80
Outer diameter of stator D_{s1} (mm)	140	Number of turns of suspension windings N	100
Length of air gap g_0 (mm)	1	Maximum bias current i (A)	5
Width of stator yoke c (mm)	21	Inner diameter of stator D_{sn1} (mm)	40
Arc length of pole shoe l_0 (mm)	20	Outer diameter of rotor D_{r1} (mm)	218
Thickness of PM h_{mb} (mm)	8	Inner diameter of rotor D_{r2} (mm)	142
Duty cycle of stator f_i	0.4	Height of a pole shoe d_m (mm)	1
Groove depth h_b (mm)	29		

As can be seen from Fig. 12, in addition to the height of shoulder c_m has little influence on the radial suspension force, and the other parameters of coil cavity have greater influences on the radial suspension force.

4.2. Optimization Design with Taguchi Method

Taguchi method is a local optimization method, which can realize multi-objective optimization design [26]. This method uses the orthogonal table to design experiments and defines the signal-to-noise ratio (SNR) to achieve statistical analysis. Then, the optimal combination of parameters can be obtained in the least number of experiments, and the influences of various disturbances on the product quality are reduced. Therefore, the Taguchi method is widely used in various motor designs and controls.

Larger radial suspension force and smaller iron loss are required in BHMB. Hence, the radial suspension force and iron loss are defined as the main performance indexes of BHMB in this paper. It can be seen from the above analysis, in addition to the height of shoulder c_m, the other parameters of coil cavity have greater influences on the radial suspension force. Meanwhile, the influence of the radial magnetized thickness of PM h_{mb} on the suspension force and iron loss is great. Therefore, five parameters of BHMB are selected to be optimized as shown in Table 2.

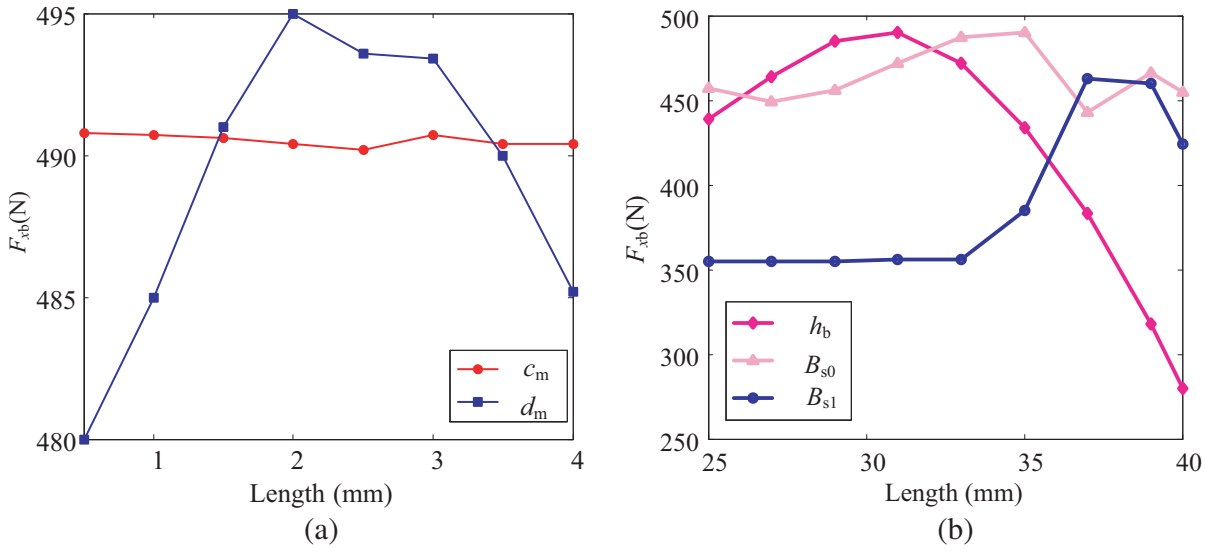

Figure 12. Relations between parameters of coil cavity and suspension force. (a) Relations between thickness, shoulder height of a pole shoe and radial suspension force. (b) Relations between slot width of rabbet, width and height of a coil cavity and radial suspension force.

Table 2. Optimal parameters and levels of BHMB.

Parameters	d_m (mm)	h_b (mm)	B_{s1} (mm)	B_{s0} (mm)	h_{mb} (mm)
Level 1	1	29	35	33	7.5
Level 2	1.5	30.5	36.5	34	8
Level 3	2	32	38	35	8.5

Table 3. Experimental array and results of FEA.

Numbers	Experimental array					Maximum radial suspension force F_x (N)	Iron loss (W)
	d_m	h_b	B_{s1}	B_{s0}	h_{mb}		
1	1	1	1	1	2	686.60	31.71
2	1	2	2	2	1	741.86	31.16
3	1	3	3	3	3	689.18	26.24
4	2	1	2	3	1	762.49	32.52
5	2	2	3	1	2	646.93	24.71
6	2	3	1	2	3	671.40	29.48
7	3	1	3	2	3	688.80	26.8
8	3	2	1	3	2	701.47	30.53
9	3	3	2	1	1	657.17	25.50

The L_9 (3^5) orthogonal array is used to construct the control matrix and design the experiment scheme. The experimental matrix and FEA results of BHMB are shown in Table 3, where 1, 2, and 3 in experimental array are the corresponding levels of each parameter, respectively. The iron loss in Table 3 includes the stator and rotor iron losses, and the speed of rotor is set to 800 r/min to simulate the actual speed of wind turbine.

Then the average and variance values of each performance index in BHMB are deduced with the statistical method. The influences of each parameter on the performance index of BHMB are analyzed.

(1) Average value of each performance index

The average value of performance indexes including suspension force and iron loss can be calculated with the following equation:

$$m(S) = \frac{1}{n}\sum_{i=1}^{n} S_i \tag{41}$$

where m is the average value of each performance index, S_i the value of each performance index calculated by FEA with different combinations of parameters, and n the number of experiments. Then, the average of each performance index is deduced as follows:

$$m_{Fx}(S) = 693.99\,\mathrm{N} \tag{42}$$

$$m_{Fe}(S) = 28.74\,\mathrm{N} \tag{43}$$

where m_{Fx} is the average value of maximum suspension force, and m_{Fe} is the average value of iron loss.

According to Table 3, the average values of the two performance indexes relative to each parameter are calculated as in Table 4. Taking the average value of radial maximum suspension force F_x with level 1 of d_m as an example, the calculation equation is given as follows:

$$m_{d_m}(F_x) = \frac{1}{3}[F_x(1) + F_x(2) + F_x(3)] \tag{44}$$

where $F_x(1)$, $F_x(2)$, and $F_x(3)$ are the maximum radial suspension forces obtained by FEA when the level of d_m is 1.

Table 4. Average values of two performance indexes in BHMB.

Parameters	Level	Radial suspension force F_x (N)	Iron loss (W)	Parameters	Level	Radial suspension force F_x (N)	Iron loss (W)
d_m	1	705.88	29.70	B_{s0}	1	663.57	27.31
	2	693.61	28.90		2	700.69	29.15
	3	682.48	27.61		3	717.71	29.76
h_b	1	712.63	30.34	h_{mb}	1	720.51	29.72
	2	696.75	28.80		2	678.33	28.98
	3	672.58	27.07		3	683.13	27.51
B_{s1}	1	686.49	30.57				
	2	720.51	29.73				
	3	674.97	25.92				

The average value of each performance index under the other parameters with the different levels can be deduced as in the above Equation (44).

(2) Proportion of each parameter to the two performance indexes

The influence of each parameter to the two performance indexes can be calculated by the following equation:

$$\mathrm{SN} = \frac{1}{3}\sum_{i=1}^{3} [m_{x_i}(S_i) - m(S)]^2 \tag{45}$$

where x_i is the parameter, $m_{xi}(S_i)$ the average value of the performance index under the parameter x with the level i, and $m(S)$ the average value of each performance index with nine experiments, as shown in Eqs. (42) and (43).

Table 5. Proportion of each parameter to the two performance index.

Parameters	Radial force F_x		Iron loss	
	SN	Proportion (%)	SN	Proportion (%)
d_m	91.33	5.78	0.74	8.67
h_b	271.15	17.15	1.78	20.87
B_{s1}	373.77	23.65	4.09	47.95
B_{s0}	510.97	32.32	1.08	12.66
h_{mb}	333.50	21.10	0.84	9.85
Total	1580.72	100	8.53	100

The proportions of each parameter to the two performance indexes are deduced as in Table 5. As seen from Table 5, the change of slot width of rabbet B_{s0} has the largest influence on the maximum radial suspension force, and the proportion is 32.32%. The change of B_{s1} has the largest influence on the iron loss of BHMB, and the proportion is 47.95%.

To observe the influences of each parameter on the two performance indexes more intuitively, Fig. 13 and Fig. 14 show the influences of five parameters on the two performance indexes, respectively, and 1, 2, and 3 in the figures are the levels corresponding to each parameter. If the maximum radial suspension force is set as the optimal objective, the values of five parameters of BHMB are selected as follows: $d_m(1)$ (1 mm), $h_b(1)$ (29 mm), $B_{s1}(2)$ (36.5 mm), $B_{s0}(3)$ (35 mm), and $h_{mb}(1)$ (7.5 mm), respectively. If the optimal objective is set to minimize iron loss in BHMB, according to Fig. 14, the values of five parameters of BHMB are selected as follows: $d_m(3)$ (2 mm), $h_b(3)$ (32 mm), $B_{s1}(3)$ (38 mm), $B_{s0}(1)$ (33 mm), and $h_{mb}(2)$ (8 mm), respectively.

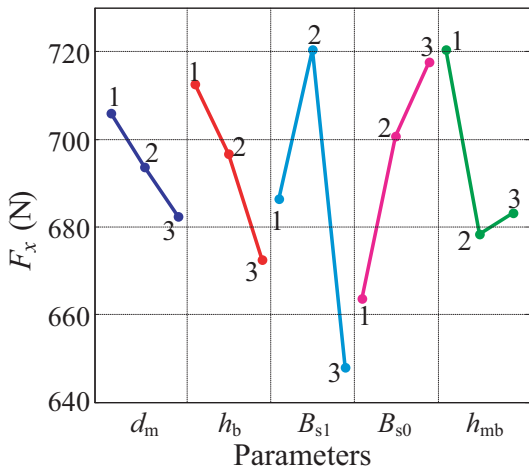

Figure 13. Influences of parameters on radial maximum suspension force F_x with different levels.

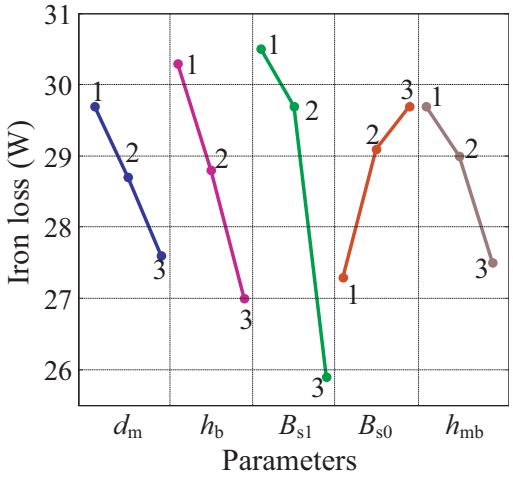

Figure 14. Influence of parameters to total iron loss at different levels.

The above analysis shows that the choices of parameters are always contradictory when the two different performance indexes of BHMB are taken as the optimal objectives. In order to obtain larger radial suspension force and smaller iron loss, the values of parameters can be chosen according to the proportions of each parameter in Table 5. The more reasonable combination of parameters can be valued as follows: $d_m(3)$ (2 mm), $h_b(3)$ (32 mm), $B_{s1}(3)$ (38 mm), $B_{s0}(3)$ (35 mm), and $h_{mb}(1)$ (7.5 mm). With the values of above parameters, the results of two performance indexes using FEA are 727.20 N and 27.01 W, respectively. Thereby using the Taguchi method, the parameters of BHMB in Table 5 are modified as shown in Table 6. And the height of shoulder c_m is 2 mm.

Table 6. Optimization results using Taguchi method.

Parameters	Values	Parameters	Values
Outer diameter of stator D_{s1} (mm)	140	Groove depth h_b (mm)	32
Width of stator yoke c (mm)	16	Axial length of stator l_1 (mm)	80
Thickness of PM h_{mb} (mm)	7.5	Height of a pole shoe d_m (mm)	2
Arc length of pole shoel_0(mm)	19.8		

5. SIMULATIONS AND EXPERIMENTAL VALIDATIONS

5.1. Verification of Flux-Insulation Effect

In order to analyze the performance of the BHMB and verify the correctness of the model of radial suspension forces, the FEA model of BHMB is built by FEA software. To verify the flux-insulation effect of the distributed hollow rotor, two same size PM motors and BHMB with only different rotor structures are constructed. One of these two rotor structures is a distributed hollow rotor, and the other is a solid rotor. The magnetic lines of fluxes of two structures with different rotors are shown in Fig. 15.

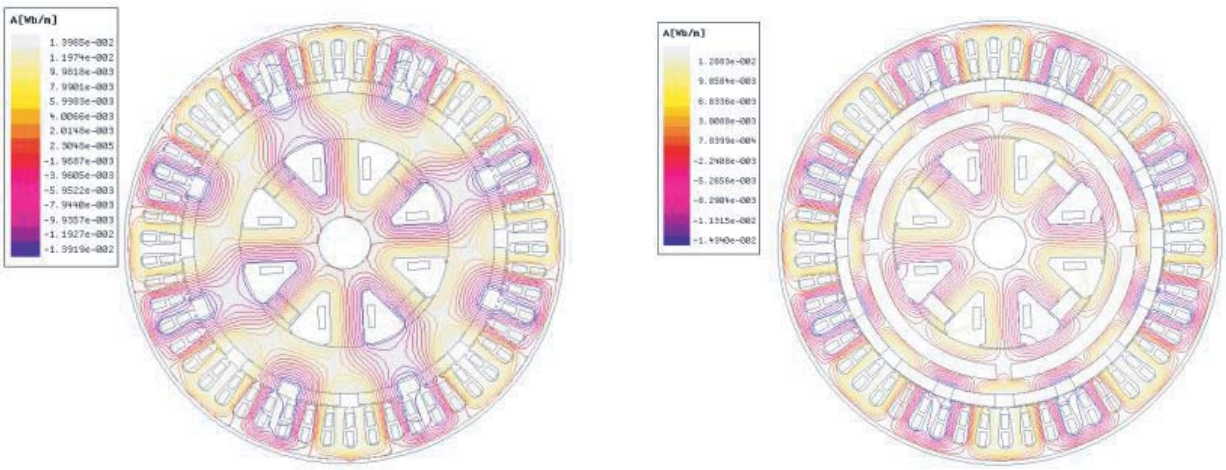

(a) (b)

Figure 15. Waveforms of magnetic line of flux with different rotor structures. (a) Solid rotor structure. (b) The distributed hollow rotor structure.

As can be seen from Fig. 15(a), using the solid rotor structure, the bias magnetic field produced by the BHMB is obviously coupled with the magnetic field generated by the PMs of the external PM motor. However, using distributed hollow rotor, there is almost no coupling between the internal and external magnetic field as shown in Fig. 15(b). The flux-insulation effect of the distributed hollow rotor structure is verified.

5.2. Rationality Verification of Suspension Windings

Taking the suspension force in x direction for example, when the suspension control currents with differential control (the same amplitude 5 A and the opposite direction) are loaded to the corresponding control windings in $+x$ and $-x$ directions, the magnetic field distribution of the BHMB is shown as in Fig. 16. It can be seen from Fig. 16(a) that the flux density in the left air gap is obviously larger than the flux density in the right air gap. As shown in Fig. 16(b), the amplitude of flux density corresponding

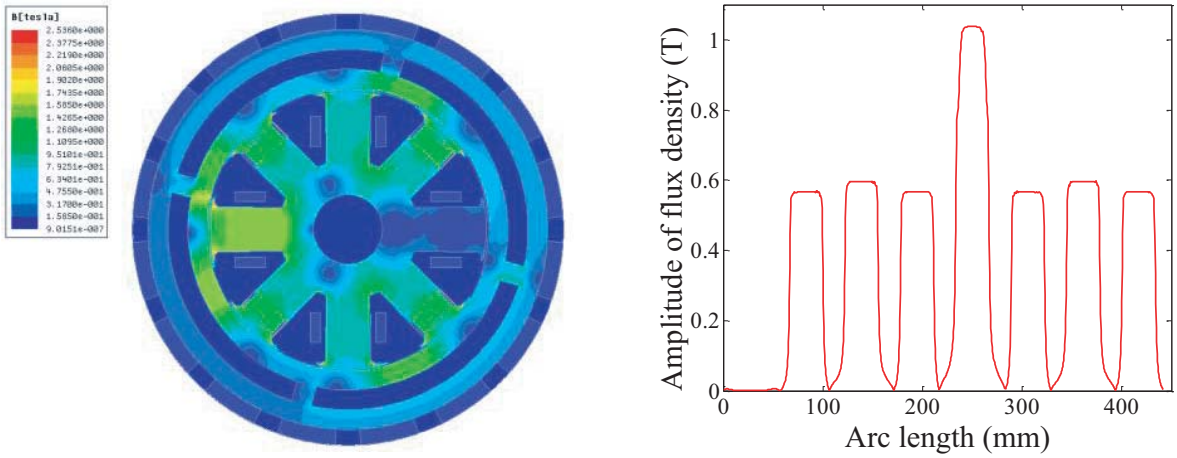

(a) (b)

Figure 16. Magnetic field distribution of radial control windings with differential control. (a) Diagram of flux density distribution with differential control. (b) Amplitude of flux density with differential control.

to one suspension control pole is significantly enhanced, and the amplitude of the other air gap is almost zero when the currents with same amplitude and opposite direction are loaded to the corresponding control windings.

As the speed of rotor is set to 375 r/min and the maximum suspension control current 5 A loaded in the $-x$ direction, the suspension forces on the rotor in x and y directions are shown in Fig. 17. As can be seen from Fig. 17, the radial suspension force in x direction is about 783 N when the suspension control windings in $-x$ direction are energized with the maximum current 5 A. The maximum force on the rotor in the y direction is about 0.4 N because the suspension control windings is not energized. Meanwhile, it can be seen that the coupling between the suspension control windings in x and y directions is very small.

To verify the correctness of the mathematical model of suspension force deduced in above section, the FEA of BHMB in magnetostatic and transient field is carried out, respectively. When the control current is changed from -4 A to 4 A and the rotation angle of rotor is 0, the comparison curves between the FEA results and the mathematical model of suspension force in the x direction are shown in Fig. 18.

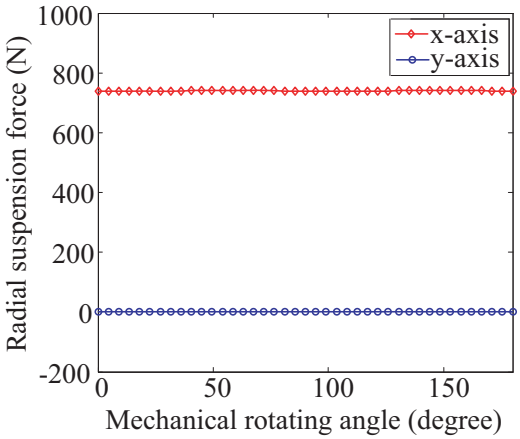

Figure 17. Radial suspension force on the rotor with maximum control current 5 A in $-x$ direction.

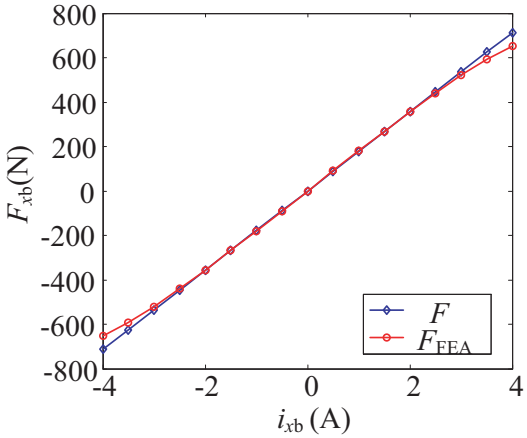

Figure 18. Comparison curves between the FEA results and the mathematical model in magnetostatic field.

F is the value of the mathematical model of suspension force in x direction, and F_{FEA} is the value of the FEA software. It can be seen that the two comparison curves basically coincide with each other when the rotor is stationary.

As the control current loaded in $-x$ direction is set as 1.3 A and 2.8 A, and the speed of rotor is at the rated speed 375 r/min, the comparison curves between FEA results and the mathematical model results are shown in Fig. 19. It can be seen that the values of FEA in x direction are basically consistent with the calculated values of the mathematical model. Thus, the correctness of Eqs. (37) and (38) can be verified.

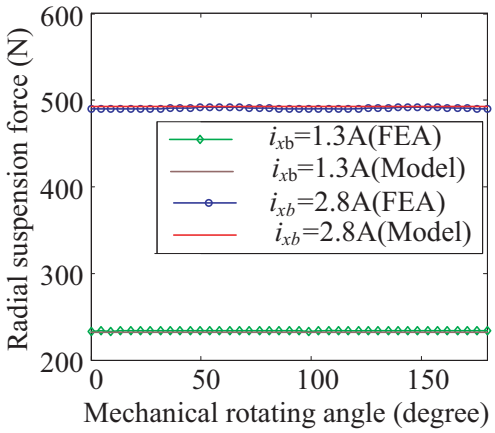

Figure 19. Comparison curves between the FEA values and the mathematical model in transient field.

5.3. Experimental Validation

To further verify the validity of the BHMB and the proposed Taguchi method, the prototype of BHMB is manufactured as shown in Fig. 20. Fig. 20(a) shows the stator of external PM motor, and the prototype of BHMB proposed in this paper is shown in Fig. 20(b).

(a) (b)

Figure 20. Prototype of PM motor and BHMB. (a) Stator of external PM motor. (b) Prototype of BHMB.

The dynamic stability of rotor is tested by the floating characteristics of rotor. The startup displacement curves of the rotor tested by two displacement sensors are shown in Fig. 21. From Fig. 21, the rotor is pulled back to the radial equilibrium position from the initial position at approximately $t = 0.18$ s. It can be seen that the rotor can quickly return to the balance position in radial direction after a short period of shock.

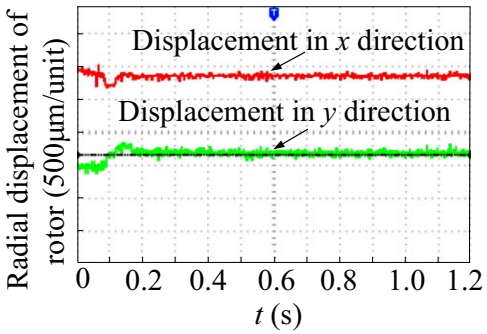

Figure 21. Startup displacement curves of rotor.

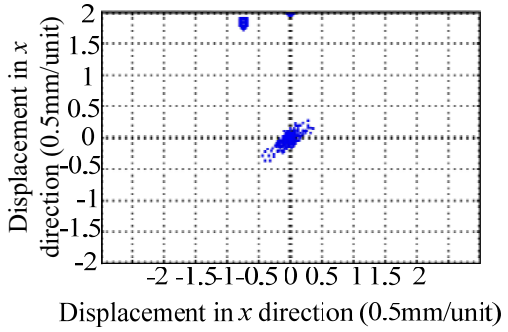

Figure 22. Radial motion trajectory of rotor at the stable suspension state.

As can be seen from Fig. 22, the x and y axes represent the displacements of the rotor in x and y directions. Each unit in Fig. 22 represents the displacement length of 0.5 mm. Although there are fluctuations in both directions, the radial displacements in x and y directions near the equilibrium position are very small (the maximum displacements in both directions shall not exceed 0.5 mm). So the rotor supported by BHMB can achieve stable suspension in stable sate.

The dynamic stability of BHMB is tested by the disturbance experiment in this paper. The experiment is arranged as follows: when the rotor is rotated at the rated speed 375 r/min and stably suspended in the balance position, a mallet is used to strike the external shaft as an external disturbance, then the change of rotor displacement is observed. Fig. 23 shows the changes of rotor displacements in radial directions when the external disturbances are applied to the rotor. From Fig. 23, it can be seen that the displacements of rotor in x and y directions are shifted when the mallet is used to strike the external shaft at $t = 0.6$ s. Then the rotor returns back to the equilibrium position at $t = 0.9$ s after the strike.

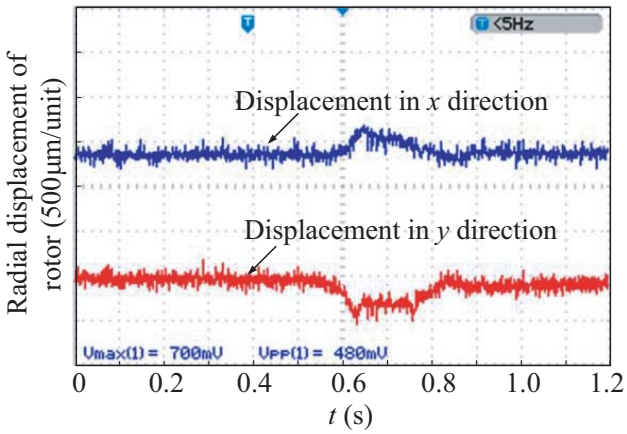

Figure 23. Displacement waves of the rotor at the disturbance test.

6. CONCLUSION

To reduce the axial length of the system, a BHMB is proposed in this paper. The BHMB sharing a disturbed hollow rotor with the external PM motor built in the horizontal axis wind turbine. The basic structure and principle of BHMB are illustrated, then the mathematic models of suspension forces are deduced. The larger radial suspension force and smaller iron loss are defined as the main performance indexes, and Taguchi method is used for the optimization design of BHMB. After optimization, the flux-insulation effect and electromagnetic performances of BHMB are verified with FEA. Finally, a prototype

is manufactured to evaluate the performances of BHMB. The results of dynamic stable experiments verify the correctness of BHMB.

REFERENCES

1. Soni, T., J. K. Dutt, and A. S. Das, "Parametric stability analysis of active magnetic bearing supported rotor system with a novel control law subject toperiodic base motion," *IEEE Transactions on Industrial Electronics*, Vol. 67, No. 2, 1160–1170, 2020.
2. Zhang, W., H. Yang, L. Cheng, and H. Zhu, "Modeling based on exact segmentation of magnetic field for a centripetal force type-magnetic bearing," *IEEE Transactions on Industrial Electronics*, Vol. 67, No. 9, 7691–7701, 2020.
3. Bekinal, S. I. and M. Doddamani, "Optimum design methodology for axially polarized multi-ring radial and thrust permanent magnei bearings," *Progress In Electromagnetics Research B*, Vol. 88, No. 3, 197–215, 2020.
4. Debnath, S. and P. K. Biswas, "Design, analysis, and testing of I-type electromagnetic actuator used in single-coil active magnetic bearing," *Electrical Engineering*, Vol. 4, 2020.
5. Ye, X., Q. Le, and Z. Zhou, "A novel homopolar four degrees of freedom hybrid magnetic bearing," *IEEE Transactions on Magnetics*, Vol. 26, No. 8, 2020.
6. Zhong, Y., L. Wu, X. Huang, and Y. Fang, "Modeling and design of a 3-DOF magnetic bearing with toroidal radial control coils," *IEEE Transactions on Magnetics*, Vol. 55, No. 7, 2019.
7. Yu, Y., W. Zhang, Y. Sun, and P. Xu, "Basic characteristics and design of a novel hybrid magnetic bearing for wind turbines," *Energies*, Vol. 9, No. 11, 2016.
8. Cui, P., Q. Wang, G. Zhang, and Q. Cao, "Hybrid fractional repetitive control for magnetically suspended rotor systems," *IEEE Transactions on Industrial Electronics*, Vol. 65, No. 4, 3491–3498, 2018.
9. Basaran, S., Sivrioglu, and Selim, "Novel repulsive magnetic bearing flywheel system with composite adaptive control," *IET Electric Power Applications*, 2019.
10. Zhou, J., S. Zheng, B. Han, and J. Fang, "Effects of notch filters on imbalance rejection with heteropolar and homopolar magnetic bearings in a 30-kW 60000-rpm motor," *IEEE Transactions on Industrial Electronics*, Vol. 64, No. 10, 8033–8041, 2017.
11. Liu, T., H. Zhu, M. Wu, and W. Zhang, "Rotor displacement self-sensing method for six-pole radial hybrid magnetic bearing using mixed-kernel fuzzy support vector machine," *IEEE Transactions on Applied Superconductivity*, Vol. 30, No. 4, 2020.
12. Zhang, T., X. Ye, L. Mo, and X. Liu, "Modeling and performance analysis on the slice hybrid magnetic bearing with two radial air-gaps," *IEEE Transactions on Applied Superconductivity*, Vol. 29, No. 2, 2019.
13. Wang, Z., T. Zhang, and S. Wu, "Suspension force analysis of four-pole hybrid magnetic bearing with large radial bearing capacity," *IEEE Transactions on Magnetics*, Vol. 56, No. 8, 2020.
14. Shrestha, G., H. Polinder, D. J. Bang, and J. A. Ferreira, "Structural flexibility: A solution for weight reduction of large direct-drive wind-turbine generators," *IEEE Trans. Energy Convers.*, Vol. 25, No. 3, 732–740, 2010.
15. Zhou, Y. and Y. Sun, "Principles and implementation of a double-stator bearingless switched reluctance starter/generator," *Proceedings of the CSEE*, Vol. 34, No. 36, 6458–6466, 2014.
16. Peng, W., Z. Xu, D. H. Lee, and J. W. Ahn, "Control of radial force in double stator type bearingless switched reluctance motor," *Journal of Electrical Engineering & Technology*, Vol. 8, No. 4, 766–772, 2013.
17. Xiang, Q. W., J. Li, Y. Yuan, and K. Chen, "Thermal modeling and analysis of hybrid excitation double stator bearingless switched reluctance motor," *Progress In Electromagnetics Research M*, Vol. 98, 137–146, 2020.

18. Xiang, Q. W., L. Feng, Y. Yu, and K. Chen, "Thermal characteristics of hybrid excitation double stator bearingless switched reluctance motor," *Progress In Electromagnetics Research C*, Vol. 101, 105–118, 2020.
19. Liu, C., X. Cao, X. Li, X. Wang, and Z. Deng, "Current delta control for conical bearingless switched reluctance motors," *2018 13th IEEE Conference on Industrial Electronics and Applications (ICIEA)*, 2075–2078, Wuhan, China, 2018.
20. Asama, J., D. Suzuki, T. Oiwa, and A. Chiba, "Development of a homo-polar bearingless motor with concentrated winding for high speed applications," *2018 International Power Electronics Conference (IPEC-Niigata 2018-ECCE Asia)*, 157–160, Niigata, Japan, 2018.
21. Higashi, H., K. Kiyota, K. Amei, and T. Ohji, "Proposal of an axial gap type single-drive bearingless reluctance motor," *2019 IEEE International Electric Machines & Drives Conference (IEMDC)*, 833–838, San Diego, CA, USA, 2019.
22. Budynas, R. and W. Young, "Roark's formulas for stress and strain," *Journal of Applied Mechanics*, Vol. 43, No. 3, 624, 2001.
23. Zhang, H., B. Kou, Y. Jin, and H. Zhang, "Modeling and analysis of a new cylindrical magnetic levitation gravity compensator with low stiffness for the 6-DOF fine stage," *IEEE Trans. Ind. Electron.*, Vol. 62, No. 6, 3629–3639, 2015.
24. Nayek, B., A. S. Das, and J. K. Dutt, "Estimation of inertial parameters of a rigid rotor having dynamic unbalance on active magnetic bearing," *Advances in Rotor Dynamics, Control, and Structural Health Monitoring*, 2020.
25. Nayek, B., A. S. Das, and J. K. Dutt, "Estimation of inertial parameters of a rigid rotor having dynamic unbalance on active magnetic bearing," *Advances in Rotor Dynamics, Control, and Structural Health Monitoring*, 2020.
26. He, J., G. Li, R. Zhou, and Q. Wang, "Optimization of permanent-magnet spherical motor based on Taguchi Method," *IEEE Transactions on Magnetics*, Vol. 56, No. 2, 2020.